



## Optimisation of air cooled, open-cathode fuel cells: Current of lowest resistance and electro-thermal performance mapping

Quentin Meyer <sup>a</sup>, Krisztian Ronaszegi <sup>a</sup>, Gan Pei-June <sup>a</sup>, Oliver Curnick <sup>b</sup>, Sean Ashton <sup>b</sup>, Tobias Reisch <sup>b</sup>, Paul Adcock <sup>b</sup>, Paul R. Shearing <sup>a</sup>, Daniel J.L. Brett <sup>a,\*</sup>

<sup>a</sup> Electrochemical Innovation Lab, Department of Chemical Engineering, UCL, London, WC1E 7JE, United Kingdom

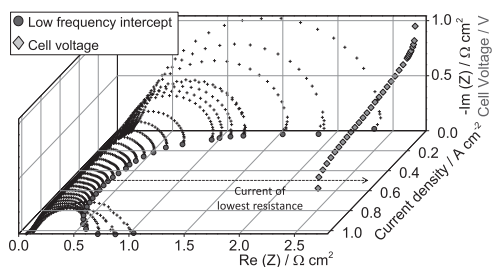
<sup>b</sup> Intelligent Energy, Charnwood Building, Holywell Park, Ashby Road, Loughborough Leicestershire, LE11 3GB, United Kingdom



### HIGHLIGHTS

- Current of lowest resistance used as a metric for performance comparison.
- Electro-thermal performance maps identify optimal performance point.
- Higher cooling flow rate increases the current of lowest resistance, and reduces the actual resistance.

### GRAPHICAL ABSTRACT



### ARTICLE INFO

#### Article history:

Received 13 August 2014

Received in revised form

14 February 2015

Accepted 16 April 2015

Available online 19 May 2015

#### Keywords:

Current of lowest resistance  
Electrochemical impedance spectroscopy  
Optimum operating temperature  
Air-cooled open-cathode polymer  
electrolyte fuel cell  
Forced convection  
Electro-thermal performance mapping

### ABSTRACT

Selecting the ideal operating point for a fuel cell depends on the application and consequent trade-off between efficiency, power density and various operating considerations. A systematic methodology for determining the optimal operating point for fuel cells is lacking; there is also the need for a single-value metric to describe and compare fuel cell performance. This work shows how the 'current of lowest resistance' can be accurately measured using electrochemical impedance spectroscopy and used as a useful metric of fuel cell performance. This, along with other measures, is then used to generate an 'electro-thermal performance map' of fuel cell operation. A commercial air-cooled open-cathode fuel cell is used to demonstrate how the approach can be used; in this case leading to the identification of the optimum operating temperature of ~45 °C.

© 2015 The Authors. Published by Elsevier B.V. This is an open access article under the CC BY license (<http://creativecommons.org/licenses/by/4.0/>).

### 1. Introduction

Polymer electrolyte fuel cells (PEFCs) fuelled with hydrogen are among the most promising energy conversion technologies

for a broad range of applications, including portable, stationary and automotive power delivery. In recent years PEFCs have shown tremendous advances in terms of performance and durability, with wide-scale commercialisation imminent. However, new techniques are sought to optimise performance by understanding the internal workings of these devices. Understanding aspects of thermal and water management is of particular interest as they have a profound effect on the performance and durability.

\* Corresponding author.

E-mail address: [d.brett@ucl.ac.uk](mailto:d.brett@ucl.ac.uk) (D.J.L. Brett).

URL: <http://www.ucl.ac.uk/electrochemical-innovation-lab>

In developing PEFC technology, it is important that appropriate comparisons are made between different operational strategies (liquid/air cooled, humidified/dry gases), designs (closed/open cathode, through-flow/dead-ended) and materials (graphitic/metallic bipolar plates, etc.). Current and voltage are the key metrics of performance; however, there is no standard metric that can report the performance of a fuel cell as a single number; rather, whole polarisation plots are typically compared. It is common to quote the current and voltage at the maximum power point in order to compare the performance between designs and operating conditions [1–7].

Whilst the maximum power density is considered to indicate the highest performance, it is obtained under extreme conditions (typ. voltage lower than 0.45 V), at a current close to the limiting current density. If operated in this region, the system is likely to undergo local dehydration and/or membrane flooding and reactant starvation. Operation at the highest current density could reduce the cell's lifetime and increase the risks of catastrophic failures [8–12]. Also, it has been shown that the fuel efficiency is less than 50% at maximum power, because the internal impedance must match the load impedance at maximum power. Operating below maximum power improves fuel efficiency [13]. The actual optimal fuel efficiency depends on the combination of the load/internal impedance ratio and the fuel recovery (recycle system) or waste (dead ended system). From a system perspective, parasitic power consumption will be higher at the maximum power density due to the heat and water management, therefore lowering the net system power [14,15]. Therefore, the maximum power is not a suitable indicator of how a fuel cell will operate under most practical conditions, and does not take into account operating parameters.

In addition, the current/voltage characteristics alone neglect a further critical parameter of performance: temperature. The temperature of a fuel cell has a profound effect on electrochemical performance, influencing the thermodynamics, electro-kinetics, transport processes and water distribution, which collectively dictate balance-of-plant requirements, system efficiency and long-term durability. It is desirable to maintain control over the stack temperature, and to minimise any inevitable heterogeneities in the temperature distribution within the stack, in order to maximise performance and durability. Therefore, the critical parameter of temperature, and indeed its spatial variation, should be considered alongside current and voltage when characterising fuel cell performance and searching for optimum operating conditions. This is important for all fuel cell types and operating modes, but is particularly relevant to air-breathing/cooled fuel cells, for which the air supply acts to provide both reactant and cooling for the system.

Air-breathing PEFCs have attracted increasing interest over the last decade. Unlike closed-cathode systems, self-breathing designs offer the advantages of simpler design and integration into systems, taking air directly from the atmosphere. Passive air-breathing systems are limited to a maximum current density of ~600 mA cm<sup>-2</sup> [1,6,16–18] due to heat and water management issues, since there is no water removal from the membrane, apart from evaporation [6,19]. Forced convection of air using fans improves performance in the so-called open-cathode configuration, and enables higher current densities to be attained [3,5,20–22].

In air-cooled, open-cathode systems the temperature depends on the voltage and current density [16,23], air cooling flow rate [3,21], and heat transfer characteristics of the stack. Temperature monitoring is therefore crucial to avoid thermal runaway or hot spot formation at high currents densities. In practice, this is normally performed using a single-point thermocouple inserted in the centre of the cell [20,24,25] or using multiple micro thermocouple measurements at various locations in the fuel cell [26–28].

Electrochemical impedance spectroscopy (EIS) is an established and powerful tool for fuel cell characterisation, providing insightful information on the various resistive losses and capacitive effects that determine fuel cell operation [29–31]. EIS has been used to characterise PEFC response to CO poisoning [32], decouple anode and cathode operation [33], and to isolate and explore the effect of specific components (e.g. platinum loading, membrane thickness, GDL structure) [29]. EIS has also found applications in localized measurements [34,35], fault detection and flooding/drying events [10,36,37], and more recently, dynamic processes such as dead-ended anode operations using a reconstructive impedance measurement technique [25]. Focusing exclusively on the high frequency intercept with the real axis of the Nyquist plot (zero phase shift point) provides a measure of the purely Ohmic impedance of a fuel cell, which can be used to measure changes in the conductivity, and therefore hydration level, of the polymer electrolyte membrane [24,37–43]. However, the low frequency intercept has been neglected as a diagnostic feature, despite representing the total impedance of the system and therefore potentially being a way to identify the minimum impedance point on the polarisation curve.

This work presents a novel approach to characterising fuel cell performance that: (i) uses the low-frequency intercept with the Nyquist plot as a means of identifying the minimum impedance point in the polarisation curve, (ii) highlights how this can be used as an optimisation strategy in order to determine the most suitable conditions, and (iii) proposes an application of this new method, in order to determine the optimum air flow rate and current density, considering the influence of the temperature as an integral part of the performance 'map', alongside current and voltage. The minimum impedance point can be used as a key performance metric. In the absence of other considerations, the minimum impedance point represents a sensible trade-off between efficiency and power, and is likely to be preferable to the maximum power point when seeking to maximise stack lifetime. 'Electro-thermal mapping' allows optimum performance regions to be identified and decouple the effect of temperature on factors such as membrane hydration (conductivity) and cooling.

## 2. Experimental

*Fuel cell testing* – A 5-cell (60 cm<sup>2</sup> active area) air-cooled/air-breathing fuel cell stack was used for testing (Intelligent Energy Ltd., UK). The membrane electrode assembly was composed of commercially available gas diffusion layers (GDLs) and commercially available membranes with Pt loading of 0.1 and 0.4 mg cm<sup>-2</sup> on the anode and cathode, respectively.

The test station supplied dry hydrogen at ambient temperature (with a purity of 99.995%) to the anodes and air was blown by three fans (SanAce 36, Sanyo Denki) to the open cathode channels [25,44]. The exhaust hydrogen flow rate in through-flow mode was measured using a thermal mass flow meter (MassVIEW, Bronkhorst) to be 4.7 SLPM. The fans, which provide cooling and air supply to the cathode, were controlled by a programmable power supply (3649A Agilent). The current drawn from the PEFC was controlled by an electronic load (PLZ664WA, Kikusui) in galvanostatic mode. An in-house computer controlled system controls the air, hydrogen, cooling and electrical valves (LabVIEW, National Instruments) as well as recording and presenting data using a data acquisition card (PCI 6221, National Instruments). It was used in the ±1 V range with a resolution down to 30 µV (i.e. 2 V/2<sup>16</sup>). Ambient temperature, pressure (absolute) and relative humidity (RH) were measured, being of around 25 °C, 1.02 bar and 40% RH respectively, during all tests. The software enables a maximum sampling rate of 5 Hz. The operation of this fuel cell in terms of open-cathode design, cooling and active channels and materials [25,44],

temperature uncertainty [44] and water management in dead-ended anode mode [25], has been described in previous reports. In this work, the anode is operated in through-flow mode and the cathode is operated in air-breathing, open-cathode configuration.

### 2.1. Electrochemical characterisation

The performance of Cell 3 was studied in detail as this is the central cell and contains a thermocouple (K-type) inserted in the centre of the cooling channel. Electrochemical impedance spectroscopy (EIS) of Cell 3 was performed using a custom made, LabVIEW-based, multichannel frequency response analyser (UCL-FRA), presented in previous work, with comparable performance to commercial software [25,45]. Impedance measurements were performed at current densities between 0 and  $1.015 \text{ A cm}^{-2}$ , within the frequency range from 3 kHz to 0.1 Hz with 10 points per decade. The amplitude of the AC perturbation was kept at 5% of the DC load. The voltages from the polarisations were measured following each impedance measurement; this ensures that the performance reported in the Nyquist, low-frequency and high-frequency profiles are consistent with the voltage measured.

## 3. Results

### 3.1. Current of lowest resistance

#### 3.1.1. Differentiation of the polarisation curve

PEFCs are typically operated at between 0.7 V and 0.55 V per cell. On the stack under investigation, the polarisation curve (Fig. 1) shows that this voltage range corresponds to a wide current density range of  $0.20 \text{ A cm}^{-2}$  –  $0.80 \text{ A cm}^{-2}$ .

From the polarisation curve, the ‘current of minimum resistance’ can be estimated by finding the minimum of the differentiated polarisation curve. The polarisation resistance is found numerically, as follows, where  $j_{-1} = j - h$  and  $j_1 = j + h$ , with  $j$  the current density, and  $h$  the current density between each step.

$$h = 3 \text{ mA cm}^{-2} \\ \frac{\Delta E}{\Delta j}(j) = \frac{E(j_1) - E(j_{-1})}{2h} \quad (1)$$

The polarisation resistance is positive whereas the polarisation curve has a negative slope: this is because the current flowing through the fuel cell is a discharge current, although plotted usually as a positive current.

As displayed in Fig. 2, the differentiated polarisation data displays a region of minimum between  $0.2$  and  $0.8 \text{ A cm}^{-2}$ . However, the accuracy with which this can be determined is limited due to scatter in the data points (signal-to-noise is defined by the absolute accuracy of  $360 \mu\text{V}$  and voltage difference measured lower than 1 mV); consequently a minimum cannot be precisely identified. In order to reduce the noise level, the differentiation was also performed using a 7-level low-noise Lanczos differentiator [46], using Equation (2),

$$\frac{\Delta E}{\Delta j_{\text{smoothed}}}(j) = -\frac{(E(j_1) - E(j_{-1})) + 2(E(j_2) - E(j_{-2})) + 3(E(j_3) - E(j_{-3}))}{28h} \quad (2)$$

With  $j_2$ ,  $j_{-2}$ ,  $j_3$  and  $j_{-3}$  defined similarly to  $j_1$  and  $j_{-1}$ , The smoothed differentiation (Fig. 2) shows a lower noise level,

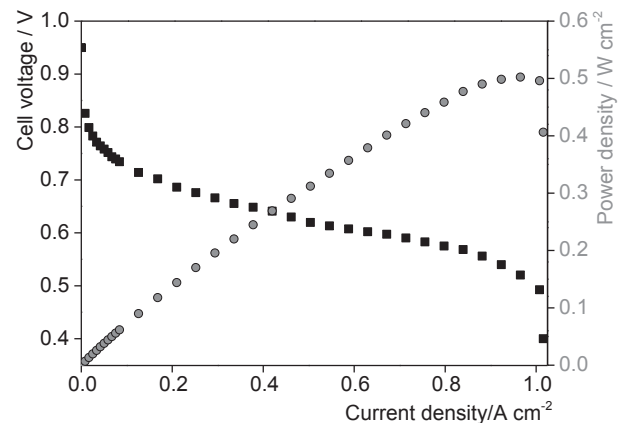


**Fig. 1.** Cell voltage and power density vs. current density for Cell 3 within the 5-cell stack.

although it does not enable to find a minimum, but slightly refines its location between  $0.25$  and  $0.75 \text{ A cm}^{-2}$

An alternative means of evaluating the minimum is by using electrochemical impedance measurements at low frequency to capture the entire resistance of the system [47,48], with a lower noise level due to the number of points processed in order to obtain the differential at a given frequency.

#### 3.1.2. Low frequency electrochemical impedance spectroscopy

Theoretically, an infinitely low frequency is required to measure the total polarisation impedance, such that the true DC (steady state) limit is reached. Some studies suggest that extrapolation to frequencies as low as  $1 \text{ nHz}$  are required to accurately obtain the total steady-state polarisation resistance of the system [29,47]. However, this is not practically feasible, just as it would not be practical to wait for  $1 \times 10^9 \text{ s}$  (over 31 years) for the fuel cell to reach ‘equilibrium’.

A number of studies have looked at the low frequency impedance of fuel cells, to obtain the total polarisation impedance [49–54]. However, a pseudo-inductive arc is commonly observed at low frequency, (such as the one observed in Fig. 3) which acts as a complicating factor. The pseudo-inductive arc has been attributed to side reactions and adsorption/desorption processes [49,52,54], the formation of hydrogen peroxide and platinum oxide, leading to platinum dissolution [50].

Accordingly, taking the point at which the Nyquist curve crosses the real axis at low frequency (as shown in Fig. 3) is not the same as measuring the total steady state (DC) resistance. Extrapolations have been performed in literature, using measurements ending at different frequencies [49–54]. However, the shape of the arc continues to evolve, even at very low frequencies, and therefore, the extrapolation does not provide a definitive low frequency limit [50,52,54].

To consider the worst operating scenario, leading to polarisation with the highest resistive losses, it was decided to look at the

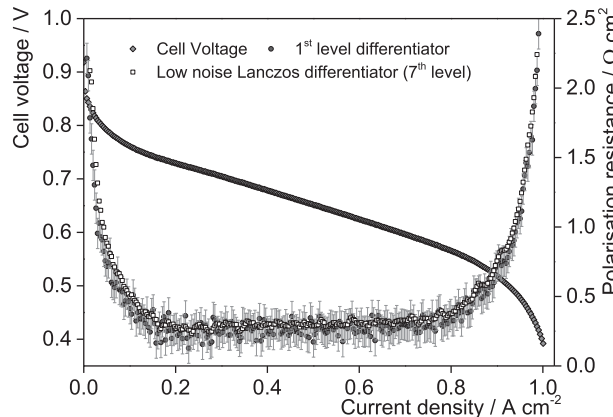


**Fig. 2.** Polarisation curve and differentiated polarisation curve (polarisation resistance) of Cell 3, using a 1st level differentiator and 7th level noise smoothing Lanczos differentiator. Current increment:  $3 \text{ mA cm}^{-2}$ . Dwell time: 5 s.

frequency providing the highest impedance on the Nyquist diagram. This is the intercept of the capacitive loop with the real axis, labelled ‘low frequency intercept’ in Fig. 3. Since at the intercept, the phase is zero, the impedance at the low frequency intercept is purely resistive, and will be referred to as the low-frequency resistance throughout the paper (similarly for the impedance at the high frequency intercept, referred to the Ohmic resistance or high-frequency resistance).

To measure the evolution of the Nyquist impedance graphs along the polarisation curve, 31 EIS measurements were made from a point close to open circuit potential ( $0.02 \text{ A cm}^{-2}$ ) to the limiting current density region ( $1.01 \text{ A cm}^{-2}$ ) (Fig. 4a). One can see features associated with three distinct regions of performance. From 0 to  $0.30 \text{ A cm}^{-2}$ , the overall impedance reduces by a factor of 6 (low frequency resistance reduces from  $2.4 \Omega \text{ cm}^2$  to  $0.4 \Omega \text{ cm}^2$ ), which corresponds to the activation losses seen on the polarisation curve. Then, the performance evolves smoothly and approximately linearly from  $0.30$  to  $0.80 \text{ A cm}^{-2}$ , associated with the ‘Ohmic region’. Finally, the overall impedance doubles above  $0.80 \text{ A cm}^{-2}$ , consistent with the drop in the mass-transport limited region of the polarisation curve.

Data fitting to equivalent circuits is extensively practiced in the literature to separate and quantify the activation, Ohmic, and mass transport contributions [29,31,49,53,55]; however, the purpose of this work is to determine the ‘current of lowest resistance’, and not the deconvolution of each losses in the total voltage loss. Fig. 4b highlights the existence of a minimum in the low-frequency intercept between at  $0.55 \text{ A cm}^{-2}$  for a resistance of  $0.348 \Omega \text{ cm}^2$ , at the centre of the Ohmic region.

As described above, the minimum impedance point on the polarisation curve represents a sensible operating point in the

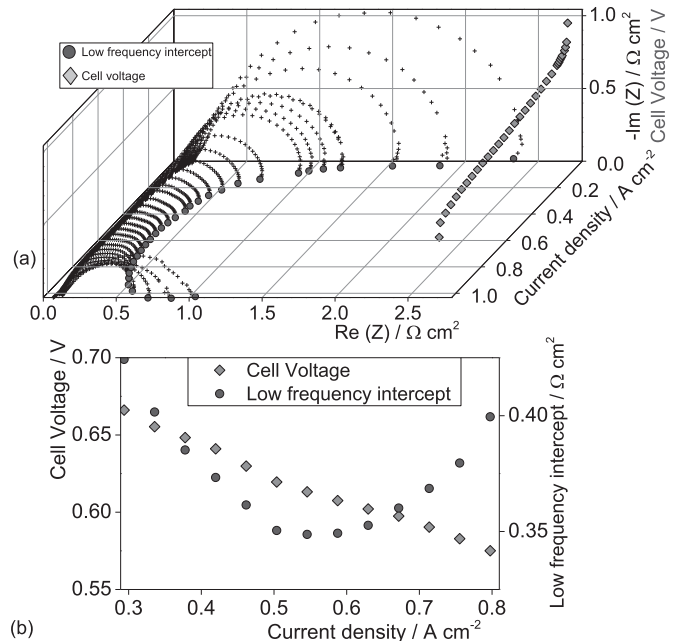


**Fig. 4.** (a) EIS measurements at 31 current steps from a point close to open circuit potential ( $0.02 \text{ A cm}^{-2}$ ) to the limiting current density ( $1.01 \text{ A cm}^{-2}$ ) along the polarisation curve, (b) Close up view on the low frequency intercept and the voltage against the current density between  $0.3$  and  $0.8 \text{ A cm}^{-2}$ .

absence of any other key performance requirement, such as a particularly high power or electrical efficiency.

The minimum impedance point of the polarisation curve or ‘current of lowest resistance’ is a useful optimisation method. It can be used to identify the optimum current density at which the fuel cell stack has minimum resistive losses (between  $0.5 \text{ A cm}^{-2}$  and  $0.6 \text{ A cm}^{-2}$  on the stack used for this study) and compare different stack designs and operating conditions in order to improve overall performance.

The following section uses this approach to examine the important link between electrochemical performance and cell/stack temperature. Such electro-thermal characterisation and optimisation is particularly important for air-cooled fuel cells where air for cooling the stack and supplying reactant oxygen come from the same source.

Performance of open-cathode air-cooled fuel cells is dependent on the flow field design (which cannot be altered in this study since a commercial stack is used), and temperature and water management [6,56]. The stack temperature is not constant, but varies with current density, and there is no external humidification regulating the hydration of the membrane. The current of lowest resistance will be used in order to determine the optimum operating conditions as a function of the cooling flow rate, current density and temperature.

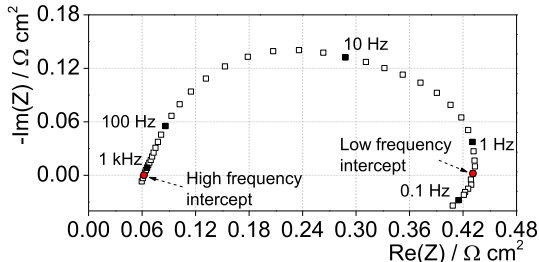


**Fig. 3.** Nyquist plot of Cell 3, with an air flow rate of  $5.35 \times 10^{-3} \text{ m}^3 \text{ s}^{-1}$  performed at  $0.3 \text{ A cm}^{-2}$ .

### 3.2. Electro-thermal performance mapping

The temperature of an air-cooled system is a result of the balance between heating from the fuel cell and the external cooling system (fans, etc.). To study this balance, the effect of varying the amount of air flowing through the active and cooling channel was studied and characterised. Then, the dependence of the temperature, voltage and current density is highlighted. Finally, the current of lowest resistance enables to determine the optimum operation mode.

### 3.2.1. Estimation of cathode and anode stoichiometry

Air-cooled, open-cathode fuel cells typically use fans to supply air to the stack. The fan speed is used to control the temperature, the cathode stoichiometry typically being in vast excess of that required. In this investigation it is necessary to know the cathode stoichiometry in order to assess the effect of varying air cooling flow rate on the performance. Directly measuring the air flow rate through an open-cathode fuel cell supplied by fans is challenging. Air is shared between active and cooling channels and the air flow rate supplied by fans is influenced by back-pressure, such that introducing flow probes or changing the configuration of the inlet plenum (or introducing an exit plenum) will affect the flow. The following section describes how an approximation of the oxygen stoichiometry can be found from a knowledge of the current passed (extent of reaction), the heat generated by the fuel cell (voltage relative to the thermal potential), difference between the air inlet/exit temperature, specific heat capacity and active/cooling channel ratio [57].

The efficiency and heat produced by the fuel cell was calculated using the following relations and the experimental data of Fig. 5a and b. The fuel cell voltage efficiency is the ratio of the cell voltage divided by the theoretical electrochemical potential.

$$\eta = \frac{V_{cell}}{E_{th}} \quad (3)$$

But the fuel cell voltage efficiency is also equal to the ratio of electrical heat losses divided by the total power losses.

$$\eta = \frac{W_{el}}{W_{el} + Q_{heat}} \quad (4)$$

$$W_{el} = A j V_{cell} N_{cells} \quad (5)$$

$\eta$  is the cell efficiency,  $V$  is the cell voltage,  $E_{th}$  is the thermal potential,  $W_{el}$  is the electrical power generated by the fuel cell and  $Q_{heat}$  the heat generated by the fuel cell.  $A$  is the electrode

geometric active area per cell,  $j$  the current density,  $V_{cell}$  the mean cell voltage and  $N_{cells}$  the number of cells in the stack.

Equations (3)–(5) allow the heat generated by the fuel cell to be calculated as a function of the electrical power (5) and the fuel cell voltage efficiency (3):

$$Q_{heat} = W_{el} \frac{1 - \eta}{\eta} \quad (6)$$

Assuming that all heat is rejected by the fuel cell in the form of convection (no radiation or conduction), the heat rejected for a given fan voltage and current density is:

$$Q_{heat}(j, T_{in}, T_{out}, V_{fan}) = \dot{m}_{air}(V_{fan}, j) C_v(T_{out} - T_{in}) \quad (7)$$

where  $\dot{m}_{air}(V_{fan}, j)$  is the volumetric air flow rate as a function of the fans' voltage  $V_{fans}$  and the current density  $j$ ,  $T_{in}$  the ambient temperature,  $T_{out}$  the exhaust temperature, and  $C_v$  the volumetric air heat capacity at 25 °C.

The volumetric air flow rate  $\dot{m}_{air}(V_{fans}, j)$  is expressed as the difference between the fans' volumetric air flow rate  $\dot{m}_{cooling}(V_{fans})$  and the volumetric oxygen conversion rate  $\dot{m}_{conversion}(j)$ .

$$\dot{m}_{air}(V_{fan}, j) = \dot{m}_{cooling}(V_{fans}) - \dot{m}_{conversion}(j) \quad (8)$$

$$\dot{m}_{conversion}(j) = \frac{jA}{n_e(O_2)F} N_{cell} V_m \quad (9)$$

where  $V_m$  is the molar volume of an ideal gas (25 °C, 1.02 bar).

The results of these calculations are shown in Fig. 5c for three different fan voltages (for a three fan system). Since a linear relation is found, one can see that  $\dot{m}_{conversion}(j)$  is negligible compared to  $\dot{m}_{cooling}(V_{fans})$ .

The corresponding voltage and air flow rates are given in Fig. 5d where it can be seen that the air flow rate varies linearly with fan voltage (specifically:  $4.20 \times 10^{-3} \text{ m}^3 \text{ s}^{-1}$ ,  $5.35 \times 10^{-3} \text{ m}^3 \text{ s}^{-1}$  and

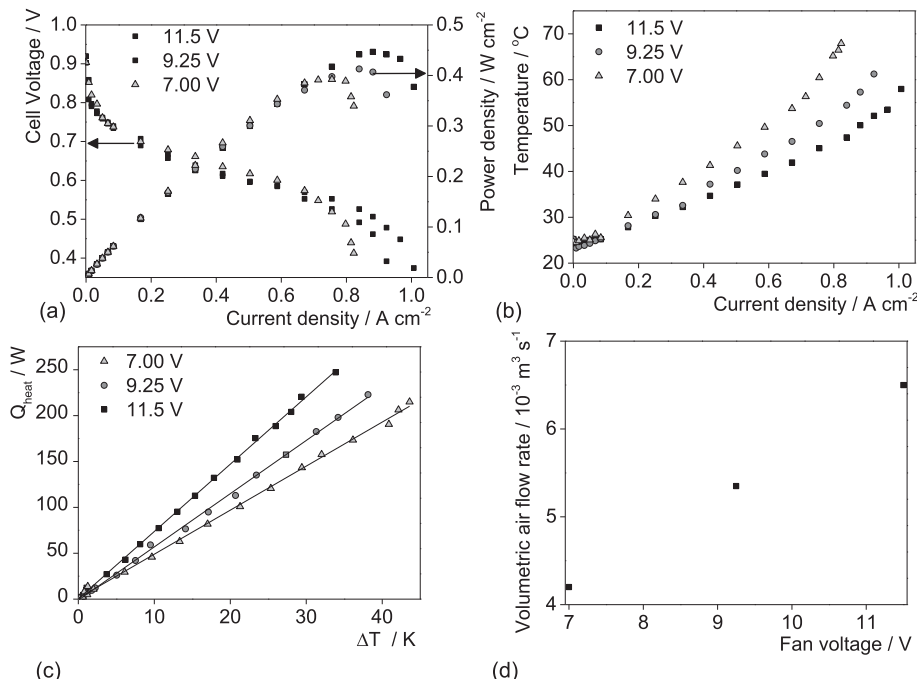


Fig. 5. (a) Voltage and power density) and (b) Temperature as a function of the fans' voltage. (c) Generated heat as a function of the temperature difference between the inlet and the exhaust of the fuel cell for the three fans' voltage. (d) Volumetric air flow rate as a function of the fans' voltage.

$6.50 \times 10^{-3} \text{ m}^3 \text{ s}^{-1}$  for voltages of 7.00 V, 9.25 V and 11.5 V, respectively).

However, this flow rate is the total amount of air passing through the active channels and cooling channels. By assuming uniform, laminar flow across the face of the cell/stack, and identical flow characteristics in active and cooling channels, the molar flow rate of oxygen through the active channels  $\dot{n}_{O_2}$  can be estimated via Equation (10).

$$\dot{n}_{O_2} = \frac{\text{Ratio of } O_2 \text{ in air}}{A_{\text{active channel}}} \frac{\dot{m}_{\text{air}}(V_{\text{fans}}, j)}{V_m} \quad (10)$$

where  $A_{\text{active channels}}$  is the total cross section area of the active channels on a cell.

Using Faraday's law, the minimum molar air flow rate required to sustain a given current density  $j$  is:

$$\dot{n}_{O_2}(j) = \frac{j}{n_e(O_2)F} AN_{\text{cells}} \quad (11)$$

Similarly, the minimum hydrogen flow rate required to sustain at a given current density  $j$  is:

$$\dot{n}_{H_2}(j) = \frac{j}{n_e(H_2)F} AN_{\text{cells}} \quad (12)$$

With  $n_e(O_2)$  the number of electrons exchanged by the oxygen reduction reaction per mole of reactant,  $n_e(H_2)$  the number of electrons exchanged by the hydrogen oxygen reactant by mole of reactant, and  $F$  Faraday's constant.

Hence, the stoichiometry ratio of oxygen at a given current density for the 5-cell stack is,

$$S_{O_2}(j) = \frac{\dot{n}_{O_2}}{\dot{n}_{O_2}(j)} \quad (13)$$

The stoichiometric ratio of hydrogen at a given current density for the 5-cell stack is,

$$S_{H_2}(j) = \frac{\dot{n}_{H_2}}{\dot{n}_{H_2}(j)} \quad (14)$$

where

$$\dot{n}_{H_2} = \frac{\dot{m}_{H_2}}{V_m} \quad (15)$$

Therefore, the stoichiometric ratio evaluated for the highest current density  $j_{\max}$ ,  $S_{O_2}(j_{\max})$  and  $S_{H_2}(j_{\max})$  can be found for oxygen and hydrogen (Equations (13) and (14)). Volumetric air flow rates of  $4.20 \times 10^{-3} \text{ m}^3 \text{ s}^{-1}$ ,  $5.35 \times 10^{-3} \text{ m}^3 \text{ s}^{-1}$  and  $6.50 \times 10^{-3} \text{ m}^3 \text{ s}^{-1}$  provide oxygen stoichiometric ratios of 27, 33 and 41 respectively at  $1 \text{ A cm}^{-2}$ . A hydrogen flow rate of 4.7 SLPM (standard litres per minute) provides a stoichiometric ratio of 2 at  $1 \text{ A cm}^{-2}$ .

Such high oxygen stoichiometries are not unusual for air-cooled open-cathode systems, Rosa et al. [3] reported oxygen stoichiometric ratios between 6.30 and 15.4 at  $0.80 \text{ A cm}^{-2}$ . These oxygen stoichiometric ratios are, as expected, much higher than the ratios used for closed-cathode system (typically between 1 and 4 [4,41,58–63]).

Table 1 summarises the parameters used in the calculation of reactant stoichiometry.

### 3.2.2. Voltage and temperature interdependence

Experiments performed previously have investigated the relationship between temperature and current density for a similar

**Table 1**

Physical constants (at 1 bar, 25 °C) and cell constants used to evaluate the oxygen and hydrogen stoichiometry.

Parameter	Value
Number of cell, $N_{\text{cells}}$	5
Membrane cross section area, $A$	$60 \text{ cm}^2$
Active channel area, $A_{\text{active channel}}$	$30 \text{ cm}^2$
Fan voltage, $V_{\text{fan}}$	$7 \text{ V} - 11.5 \text{ V}$
Faraday constant, $F$	$96486 \text{ C mol}^{-1}$
Ratio of $O_2$ in air	0.21
Number of electrons of oxygen exchanged, $n_e(O_2)$	4
Number of electrons of hydrogen exchanged, $n_e(H_2)$	2
Hydrogen volumetric flow rate,	$4.7 \text{ l min}^{-1}$
Molar volume of an ideal gas, $V_m$	$24.465 \text{ mol l}^{-1}$
Maximum current density, $j_{\max}$	$1 \text{ A cm}^{-2}$
Volumetric heat capacity of air, $C_v$	$0.001131 \text{ J cm}^{-3} \text{ K}^{-1}$

open-cathode fuel cell [25,44]. It was found that the temperature does not evolve significantly in the low current density region, increases linearly in the Ohmic region, and finally increases exponentially towards the limiting current density.

Fig. 6 describes the experimentally determined temperature, current and voltage as a function of air flow rate. By overlaying a temperature colour gradient onto the electrochemical parameters, a '4-dimensional' representation that describes an 'electro-thermal performance map' can be constructed. This graphical representation allows the effect of a control variable (in this case the air flow rate) on the three operational parameters to be observed. Studying the relationship between temperature, voltage and current is particularly relevant for air-cooled open-cathode fuel cells. Unlike for systems where the temperature is controlled to a fixed point or range, the temperature recorded here is the result of a balance between self-heating and cooling due to the fans. The air flow rate is the only control parameter for any given point on the polarisation curve.

One can see in Fig. 5b and Fig. 6 that changing the air flow rate directly affects the limiting current density. When operated with a flow rate of  $4.20 \times 10^{-3} \text{ m}^3 \text{ s}^{-1}$  the cell voltage starts to show signs of significant performance limitations around  $0.60 \text{ A cm}^{-2}$  and the current density is approximately  $0.82 \text{ A cm}^{-2}$ , (Fig. 5b); whereas such limitations only start to occur above  $0.70 \text{ A cm}^{-2}$  and  $0.90 \text{ A cm}^{-2}$  upon increasing flow rates to  $5.35 \times 10^{-3} \text{ m}^3 \text{ s}^{-1}$  and

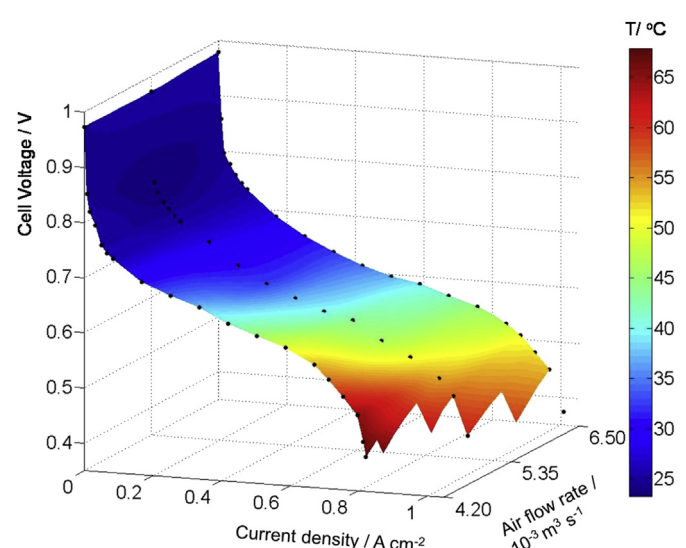


**Fig. 6.** Influence of the air flow rate on the electro-thermal performance map.

$6.50 \times 10^{-3} \text{ m}^3 \text{ s}^{-1}$ , respectively. The electro-thermal performance map (Fig. 6) highlights that the rapid change in temperature corresponds exactly with the abrupt voltage drop-off in the limiting current density region, as the temperature exceeds  $50^\circ\text{C}$ . The lowest cathode stoichiometry experienced in this set of experiments is 27, which means that oxygen is in vast excess of what is required to sustain reaction. This suggests that a thermal effect, as opposed to a reactant starvation effect, is responsible for performance limitation above  $50^\circ\text{C}$ .

If only the conventional polarisation/power curves are considered, as shown in Fig. 5a, one would infer that above  $0.70 \text{ A cm}^{-2}$ , a flow rate of  $6.50 \times 10^{-3} \text{ m}^3 \text{ s}^{-1}$  (11.5 V fan voltage) provides higher performance. However, it is not possible to see any effect of the air flow rate on the performance below  $0.70 \text{ A cm}^{-2}$ , whereas the electro-thermal performance map in Fig. 6 highlights that different operational temperatures are apparent in the Ohmic region between  $0.20$  and  $0.60 \text{ A cm}^{-2}$ , depending on the air flow rate. This demonstrates, as discussed previously, the limitations of a comparison strictly based on the maximum power density.

### 3.2.3. Effect of the cooling flow rate on the hydration level, and current of lowest resistance

For purposes of comparison, profiles similar to Fig. 6 were generated by replacing the voltage with the resistance at the high- and low-frequency intercept of the EIS response. By monitoring the high-frequency intercept with the real axis it is possible to determine the Ohmic resistance of the cell, and consequently gain an indication of the effect of the temperature and cooling flow rate on the hydration of the membrane [11,34]. Since it is an open cathode system, It is not possible to measure the humidity of the air exiting the stack.

Fig. 7a shows three different regimes for the evolution of the Ohmic resistance. Starting from the open circuit, increasing current leads to an initial decrease in resistance that is common for all of the flow rates; up to  $0.10 \text{ A cm}^{-2}$ , the resistance falls from  $225 \text{ m}\Omega \text{ cm}^2$  to  $75 \text{ m}\Omega \text{ cm}^2$ , and is associated with gradual self-hydration of the electrolyte membrane from a relatively 'dry state' at open circuit potential to a well-humidified state, since the stack operates without external humidification. From  $0.10$  to  $0.50 \text{ A cm}^{-2}$  the resistance drop decreases, eventually reaching a minimum at around  $0.50$ – $0.70 \text{ A cm}^{-2}$ . At higher current densities, the Ohmic resistance increases exponentially from  $\sim 55 \text{ m}\Omega \text{ cm}^2$  to over  $110 \text{ m}\Omega \text{ cm}^2$  at a rate that is a function of the air flow rate. However, it is only when the electro-thermal performance map is considered (Fig. 7b) that this effect can be associated with temperature.

Above  $55^\circ\text{C}$ , the Ohmic resistance increases significantly, indicating membrane dehydration. With higher air flow rates (cooling), the dehydration is delayed and occurs only above around  $0.60$ – $0.80 \text{ A cm}^{-2}$  and  $0.70$ – $0.82 \text{ A cm}^{-2}$  for flow rates of  $5.35 \times 10^{-3} \text{ m}^3 \text{ s}^{-1}$  and  $6.50 \times 10^{-3} \text{ m}^3 \text{ s}^{-1}$ , respectively. This is because the higher flow rate affords a lower temperature, limiting membrane dehydration.

Multiple studies have modelled and measured this dependence of the Ohmic resistance on current densities on passive open-cathode systems [56,64,65]. O'Hare et al. [64] also modelled how an increase in air flow rate reduces the Ohmic resistance, and increases the fuel cell resistance at a given current density, as seen here above  $0.60 \text{ A cm}^{-2}$ . To our knowledge, this is the first time high frequency impedance has been used to report it on air-cooled open-cathode systems and highlights the influence of the cooling air flow rate.

Investigations on the influence of the flow rate on the 'current of lowest resistance' were achieved by performing low frequency intercept impedance measurements of the entire current range.

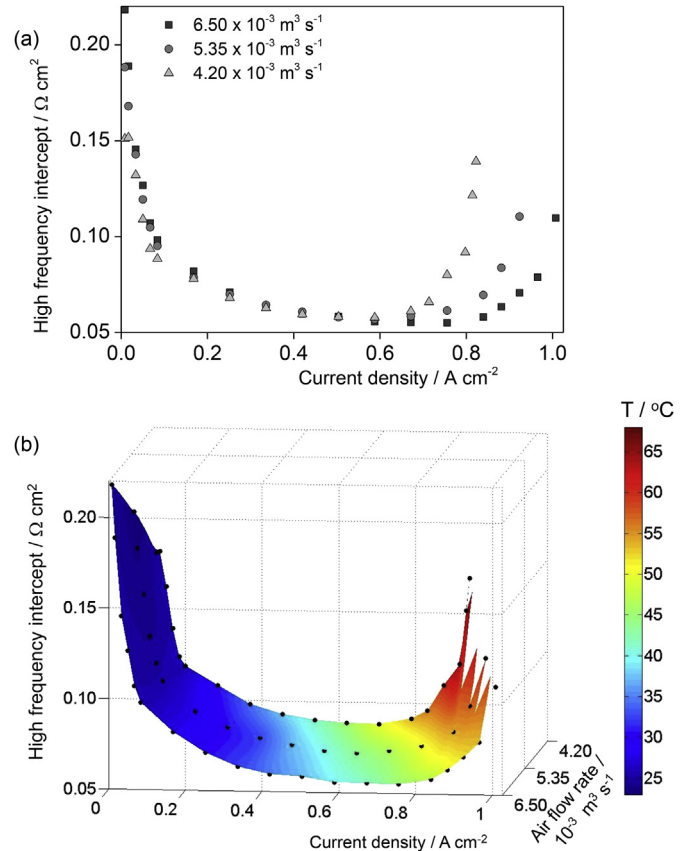
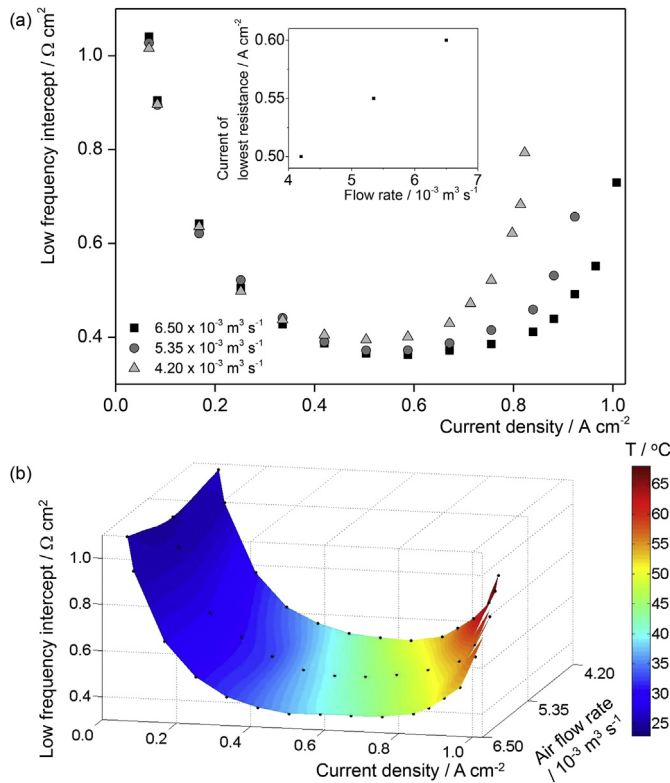


Fig. 7. (a) Influence of the air flow rate on the high-frequency resistance as a function of current density. (b) Influence of air flow rate on the electro-thermal performance map, as defined by the high-frequency resistance.

Fig. 8a shows that the 'current of lowest resistance' (defined by the minimum of the low-frequency resistance) shifts toward higher current densities with increasing flow rate; the linearity of which is shown inset. On the other hand, the electro-thermal profile, Fig. 8b, shows that the minimum remains in the same temperature region from  $45^\circ\text{C}$  to  $50^\circ\text{C}$ . One can see that the minimum of the low-frequency intercept is slightly lower than that of the high-frequency intercept: this is in agreement with O'Hare et al. [64] which implies that optimum performance is reached prior to the onset of membrane dehydration.

The low-frequency intercept increases significantly more than the purely Ohmic resistance. It is possible that severe membrane dehydration at high current density would cause a dehydration of the catalyst layers, effectively reducing the active area. Therefore, the voltage would drop to achieve the same current, which leads to a significant increase of the effective resistance for proton conduction in the cathode [66]. It is also possible that, although the channels are fed with a large stoichiometric excess of air, the land area could experience fuel starvation at high current density.

Furthermore, Fig. 8 allows the exact determination of the 'current of lowest resistance'. Fig. 8 b identifies the electro-thermal region where the main fuel cell resistive losses are minimised, around a temperature of  $\sim 45^\circ\text{C}$  and a current density between  $0.50 \text{ A cm}^{-2}$  and  $0.60 \text{ A cm}^{-2}$ . Although the effect of different flow rates shows little influence on the power density curves (Fig. 5b) between  $0.50$  and  $0.60 \text{ A cm}^{-2}$ , the low-frequency resistance efficiently shows that higher flow rates are preferable. Not only higher flow rate enables a higher current of lowest resistance, but also, the resistance itself is lower as shown in Table 2. The current of lowest



**Fig. 8.** (a) Influence of the air flow rate on the low-frequency intercept; inset: evolution of the 'current of lowest resistance' as a function of air flow rate. (b) Influence of air flow rate on the electro-thermal performance map, as defined by the low-frequency resistance.

resistance is particularly useful here, compared to the polarisations (Fig. 8b) because the three polarisations display similar voltages, in the linear region, whereas the current of lowest resistance are different.

Finally, the corresponding cell voltages at the current of lowest resistance are around 0.60 V, well within the typical operating range (0.70 V–0.55 V); whereas the voltage at the current of highest power density is around 0.50 V. This illustrates how the current of lowest resistance is a more suitable single-value metric than the maximum power point.

#### 4. Conclusion

A methodology has been proposed to identify the current of lowest resistance, using low-frequency impedance spectroscopy, in order to minimise the resistive losses and optimise the operating conditions. This point can be used as a key metric to compare the operation of different fuel cells designs and has advantages over the maximum power point. Operating the fuel cell in this region represents a sensible trade-off between fuel cell efficiency, power density and may be beneficial for durability.

**Table 2**

Current of lowest resistance, and corresponding resistance as a function of the air flow rate.

Air flow rate/ $10^{-3} \text{ m}^3 \text{s}^{-1}$	Current of lowest resistance/ $\text{A cm}^{-2}$	Resistance at the "current of lowest resistance"/ $\text{m}\Omega \text{ cm}^2$
4.20	0.50	394
5.35	0.55	371
6.50	0.60	363

This approach is applied to an air-cooled, air-breathing polymer electrolyte fuel cell stack. By constructing an 'electro-thermal performance map' based on voltage, high- and low-frequency impedance, the optimal performance region can be identified and the interrelations between temperature and electrochemical performance identified; this being particularly germane for air-cooled/air-breathing fuel cells. The analysis presented here describes a means of identifying the optimum operating region. For a system, the relationship needs to incorporate the parasitic power consumption of the fans, and its influence on the net power.

#### Acknowledgements

The authors would like to acknowledge the EPSRC for supporting Brett and his research group through (EP/G030995/1), (EP/I037024/1) and (EP/J001007/1). We acknowledge the support of Intelligent Energy and UCL for supporting the studentship of Meyer and the RAEng for supporting Shearing. Finally we acknowledge Dr. Simon Barrass for technical input in the development of the EIS system.

#### References

- N. Bussajarn, H. Ming, K.K. Hoong, W.Y. Ming Stephen, C.S. Hwa, Planar air breathing PEMFC with self-humidifying MEA and open cathode geometry design for portable applications, *Int. J. Hydrogen Energy* 34 (2009) 7761–7767.
- B.F. Laurencelle, R. Chahine, J. Hamelin, K. Agbossou, M. Fournier, T.K. Bose, et al., Characterization of a ballard MK5-E proton exchange membrane fuel cell stack, *Fuel Cells* (2001) 66–71.
- D.T.S. Rosa, D.G. Pinto, V.S. Silva, R.A. Silva, C.M. Rangel, High performance PEMFC stack with open-cathode at ambient pressure and temperature conditions, *Int. J. Hydrogen Energy* 32 (2007) 4350–4357.
- A. Li, M. Han, S.H. Chan, N. Nguyen, Effects of hydrophobicity of the cathode catalyst layer on the performance of a PEM fuel cell, *Electrochim. Acta* 55 (2010) 2706–2711.
- J. Wu, S. Galli, I. Lagana, A. Pozio, G. Monteleone, X. Zi, et al., An air-cooled proton exchange membrane fuel cell with combined oxidant and coolant flow, *J. Power Sources* 188 (2009) 199–204.
- S.U. Jeong, E.A. Cho, H.-J. Kim, T.-H. Lim, I.-H. Oh, S.H. Kim, A study on cathode structure and water transport in air-breathing PEM fuel cells, *J. Power Sources* 159 (2006) 1089–1094.
- S.U. Jeong, E.A. Cho, H.-J. Kim, T.-H. Lim, I.-H. Oh, S.H. Kim, Effects of cathode open area and relative humidity on the performance of air-breathing polymer electrolyte membrane fuel cells, *J. Power Sources* 158 (2006) 348–353.
- M. Ji, Z. Wei, A review of water management in polymer electrolyte membrane fuel cells, *Energies* 2 (2009) 1057–1106.
- P. Rama, R. Chen, J. Andrews, A review of performance degradation and failure modes for hydrogen-fuelled polymer electrolyte fuel cells, *Proc. Inst. Mech. Eng. Part A J. Power Energy* 222 (2008) 421–441.
- W. Mérida, D.A. Harrington, J.M. Le Canut, G. McLean, Characterisation of proton exchange membrane fuel cell (PEMFC) failures via electrochemical impedance spectroscopy, *J. Power Sources* 161 (2006) 264–274.
- T.J. Mason, J. Millichamp, T.P. Neville, P.R. Shearing, S. Simons, D.J.L. Brett, A study of the effect of water management and electrode flooding on the dimensional change of polymer electrolyte fuel cells, *J. Power Sources* 242 (2013) 70–77.
- J.B. Siegel, D.A. McKay, A.G. Stefanopoulou, D.S. Hussey, D.L. Jacobson, Measurement of liquid water accumulation in a PEMFC with dead-ended anode, *J. Electrochem. Soc.* 155 (2008) B1168.
- J.B. Benziger, M.B. Satterfield, W.H.J. Hogarth, J.P. Nehls, I.G. Krevrekidis, The power performance curve for engineering analysis of fuel cells, *J. Power Sources* 155 (2006) 272–285.
- S. Yu, D. Jung, Thermal management strategy for a proton exchange membrane fuel cell system with a large active cell area, *Renew. Energy* 33 (2008) 2540–2548.
- R. Flückiger, A. Tiefenauer, M. Ruge, C. Aebi, A. Wokaun, F.N. Büchi, Thermal analysis and optimization of a portable, edge-air-cooled PEFC stack, *J. Power Sources* 172 (2007) 324–333.
- A. Schmitz, M. Tranitz, S. Wagner, R. Hahn, C. Hebling, Planar self-breathing fuel cells, *J. Power Sources* 118 (2003) 162–171.
- R. Hahn, S. Wagner, A. Schmitz, H. Reichl, Development of a planar micro fuel cell with thin film and micro patterning technologies, *J. Power Sources* 131 (2004) 73–78.
- S.U. Jeong, E.A. Cho, H.-J. Kim, T.-H. Lim, I.-H. Oh, S.H. Kim, Effects of cathode open area and relative humidity on the performance of air-breathing polymer electrolyte membrane fuel cells, *J. Power Sources* 158 (2006) 348–353.
- T. Fabian, R. O'Hare, S. Litster, F.B. Prinz, J.G. Santiago, Passive water

- management at the cathode of a planar air-breathing proton exchange membrane fuel cell, *J. Power Sources* 195 (2010) 3201–3206.
- [20] G. Jung, K. Lo, A. Su, F. Weng, C. Tu, T. Yang, et al., Experimental evaluation of an ambient forced-feed air-supply PEM fuel cell, *Int. J. Hydrogen Energy* 33 (2008) 2980–2985.
- [21] A.P. Sasmito, E. Birgersson, K.W. Lum, A.S. Mujumdar, Fan selection and stack design for open-cathode polymer electrolyte fuel cell stacks, *Renew. Energy* 37 (2012) 325–332.
- [22] B. Kim, Y. Lee, A. Woo, Y. Kim, Effects of cathode channel size and operating conditions on the performance of air-blowing PEMFCs, *Appl. Energy* 111 (2013) 441–448.
- [23] T. Fabian, J.D. Posner, R. O'Hayre, S.-W. Cha, J.K. Eaton, F.B. Prinz, et al., The role of ambient conditions on the performance of a planar, air-breathing hydrogen PEM fuel cell, *J. Power Sources* 161 (2006) 168–182.
- [24] O. Lottin, T. Colinart, S. Chupin, S. Didierjean, A multi-instrumented polymer exchange membrane fuel cell: observation of the in-plane non-homogeneities, *J. Power Sources* 180 (2008) 748–754.
- [25] Q. Meyer, S. Ashton, O. Curnick, T. Reisch, P. Adcock, K. Ronaszegi, et al., Dead-ended anode polymer electrolyte fuel cell stack operation investigated using electrochemical impedance spectroscopy, off-gas analysis and thermal imaging, *J. Power Sources* 254 (2013) 1–9.
- [26] M. Wilkinson, M. Blanco, E. Gu, J.J. Martin, D.P. Wilkinson, J.J. Zhang, et al., In situ experimental technique for measurement of temperature and current distribution in proton exchange membrane fuel cells, *Fuel Cell.* 9 (2006) 507–511.
- [27] H. Guo, M. Hai, F. Ye, C. Fang, Experimental study of temperature distribution on anodic surface of MEA inside a PEMFC with parallel channels flow bed, *Int. J. Hydrogen Energy* 37 (2012) 13155–13160.
- [28] C. Wen, G. Huang, Application of a thermally conductive pyrolytic graphite sheet to thermal management of a PEM fuel cell, *J. Power Sources* 178 (2008) 132–140.
- [29] X. Yuan, H. Wang, J. Colinsun, J. Zhang, AC impedance technique in PEM fuel cell diagnosis—A review, *Int. J. Hydrogen Energy* 32 (2007) 4365–4380.
- [30] M.U. Iftikhar, D. Riu, F. Druart, S. Rosini, Y. Bultel, N. Retière, Dynamic modeling of proton exchange membrane fuel cell using non-integer derivatives, *J. Power Sources* 160 (2006) 1170–1182.
- [31] S.M. Rezaei Niya, M. Hoofar, Study of proton exchange membrane fuel cells using electrochemical impedance spectroscopy technique — A review, *J. Power Sources* 240 (2013) 281–293.
- [32] J. Kim, Y. Park, K. Kobayashi, M. Nagai, Characterization of CO tolerance of PEMFC by ac impedance spectroscopy, *Solid State Ionics* (2001) 313–325.
- [33] H. Kuhn, B. Andreus, A. Wokaun, G.G. Scherer, Electrochemical impedance spectroscopy applied to polymer electrolyte fuel cells with a pseudo reference electrode arrangement, *Electrochim. Acta* 51 (2006) 1622–1628.
- [34] D.J.L. Brett, S. Atkins, N.P. Brandon, N. Vasileiadis, V. Vesovic, A.R. Kucernak, Membrane resistance and current distribution measurements under various operating conditions in a polymer electrolyte fuel cell, *J. Power Sources* 172 (2007) 2–13.
- [35] D.J.L. Brett, S. Atkins, N.P. Brandon, V. Vesovic, N. Vasileiadis, A. Kucernak, Localized impedance measurements along a single channel of a solid polymer fuel cell, *Electrochim. Solid-State Lett.* 6 (2003) A63.
- [36] J.-M. Le Canut, R.M. Abouatallah, D.A. Harrington, Detection of membrane drying, fuel cell flooding, and anode catalyst poisoning on pemfc stacks by electrochemical impedance spectroscopy, *J. Electrochim. Soc.* 153 (2006) A857.
- [37] T. Kurz, A. Hakenjos, J. Krämer, M. Zedda, C. Agert, An impedance-based predictive control strategy for the state-of-health of PEM fuel cell stacks, *J. Power Sources* 180 (2008) 742–747.
- [38] D. Gerteisen, N. Zamel, C. Sadeler, F. Geiger, V. Ludwig, C. Hebling, Effect of operating conditions on current density distribution and high frequency resistance in a segmented PEM fuel cell, *Int. J. Hydrogen Energy* 37 (2012) 7736–7744.
- [39] T. Matsuura, J. Chen, J.B. Siegel, A.G. Stefanopoulou, Degradation phenomena in PEM fuel cell with dead-ended anode, *Int. J. Hydrogen Energy* 38 (2013) 11346–11356.
- [40] J. Pino, F. Rosa, A. Irazo, M. Mun, E. Lo, Experimental fuel cell performance analysis under different operating conditions and bipolar plate designs, *Int. J. Hydrogen Energy* 5 (2010) 11437–11447.
- [41] D. Gerteisen, W. Mérida, T. Kurz, P. Lupotto, M. Schwager, C. Hebling, Spatially resolved voltage, current and electrochemical impedance spectroscopy measurements, *Fuel Cells* 11 (2011) 339–349.
- [42] S.J.C. Cleghorn, D.K. Mayfield, D.A. Moore, J.C. Moore, G. Rusch, T.W. Sherman, et al., A polymer electrolyte fuel cell life test : 3 years of continuous operation, *J. Power Sources* 158 (2006) 446–454.
- [43] A. Hakenjos, C. Hebling, Spatially resolved measurement of PEM fuel cells, *J. Power Sources* 145 (2005) 307–311.
- [44] M. Noorkami, J.B. Robinson, Q. Meyer, O.A. Obeisun, E.S. Fraga, T. Reisch, et al., Effect of temperature uncertainty on polymer electrolyte fuel cell performance5, *Int. J. Hydrogen Energy* 39 (2014) 1439–1448.
- [45] Q. Meyer, S. Barass, O. Curnick, T. Reisch, D.J.L. Brett, A multichannel frequency response analyser for impedance spectroscopy on power sources, *J. Electrochem. Sci. Eng.* 3 (2013) 107–114.
- [46] P. Holoborodko [http://www.holoborodko.com/pavel/numerical-methods/numerical-derivative/lanczos-low-noise-differentiators/#lanczos\\_2](http://www.holoborodko.com/pavel/numerical-methods/numerical-derivative/lanczos-low-noise-differentiators/#lanczos_2), (accessed 28.07.2014) (2002).
- [47] N. Wagner, Characterization of membrane electrode assemblies in polymer electrolyte fuel cells using a.c. impedance spectroscopy, *J. Appl. Electrochem.* (2002) 859–863.
- [48] Y. Tang, J. Zhang, C. Song, H. Liu, J. Zhang, H. Wang, et al., Temperature dependent performance and in situ ac impedance of high-temperature PEM fuel cells using the nafion-112 membrane, *J. Electrochim. Soc.* 153 (2006) A2036.
- [49] M. Mathias, D. Baker, W. Gu, M. Murphy, K. Neyerlin, Low Frequency Impedance Of Polymer Electrolyte Fuel Cells, *Meet. Abstr.* MA2005-01, 2006, p. 1519.
- [50] S.K. Roy, M.E. Orazem, B. Tribollet, Interpretation of low-frequency inductive loops in PEM fuel cells, *J. Electrochim. Soc.* 154 (2007) B1378.
- [51] I.A. Schneider, M.H. Bayer, A. Wokaun, G.G. Scherer, Impedance response of the proton exchange membrane in polymer electrolyte fuel cells, *J. Electrochim. Soc.* 155 (2008) B783.
- [52] R. Makharia, M.F. Mathias, D.R. Baker, Measurement of catalyst layer electrolyte resistance in pefcs using electrochemical impedance spectroscopy, *J. Electrochim. Soc.* 152 (2005) A970.
- [53] A.M. Dhir, N.V. Dale, H. Salehfar, M.D. Mann, T. Han, Equivalent electric circuit modeling and performance analysis of a pem fuel cell stack using impedance spectroscopy, *IEEE Trans. Energy Convers.* 25 (2010) 778–786.
- [54] S. Cruz-Manzo, R. Chen, An electrical circuit for performance analysis of polymer electrolyte fuel cell stacks using electrochemical impedance spectroscopy, *J. Electrochim. Soc.* 160 (2013) F1109–F1115.
- [55] D.A. Harrington, P. van den Driessche, Mechanism and equivalent circuits in electrochemical impedance spectroscopy, *Electrochim. Acta* 56 (2011) 8005–8013.
- [56] M. Paquin, L.G. Fréchette, Understanding cathode flooding and dry-out for water management in air breathing PEM fuel cells, *J. Power Sources* 180 (2008) 440–451.
- [57] C. Spiegel, *PEM Fuel Cell Modelling and Simulation Using MATLAB*, Elsevier, 2008.
- [58] Y. Sohn, G. Park, T. Yang, Y. Yoon, W. Lee, S. Yim, et al., Operating characteristics of an air-cooling PEMFC for portable applications, *J. Power Sources* 145 (2005) 604–609.
- [59] X. Yan, M. Hou, L. Sun, D. Liang, Q. Shen, H. Xu, et al., AC impedance characteristics of a 2kW PEM fuel cell stack under different operating conditions and load changes, *Int. J. Hydrogen Energy* 32 (2007) 4358–4364.
- [60] M. Sousa, L.C. Pe, Segmented polymer electrolyte membrane fuel cells — A review, *Renew. Sustain. Energy Rev.* 15 (2011) 169–185.
- [61] K. Hauer, R. Potthast, W. Thorsten, Magnetotomography — a new method for analysing fuel cell performance and quality, *Situ* 143 (2005) 67–74.
- [62] Z. Qi, H. Tang, Q. Guo, B. Du, Investigation on "saw-tooth" behavior of PEM fuel cell performance during shutdown and restart cycles, *J. Power Sources* 161 (2006) 864–871.
- [63] M. Boillot, C. Bonnet, S. Didierjean, F. Lapicque, Investigation of the response of separate electrodes in a polymer electrolyte membrane fuel cell without reference electrode, *J. Appl. Electrochim* 37 (2007) 103–110.
- [64] R. O'Hayre, T. Fabian, S. Litster, F.B. Prinz, J.G. Santiago, Engineering model of a passive planar air breathing fuel cell cathode, *J. Power Sources* 167 (2007) 118–129.
- [65] T. Fabian, J.D. Posner, R. O'Hayre, S.-W. Cha, J.K. Eaton, F.B. Prinz, et al., The role of ambient conditions on the performance of a planar, air-breathing hydrogen PEM fuel cell, *J. Power Sources* 161 (2006) 168–182.
- [66] K.C. Neyerlin, W. Gu, J. Jorne, A. Clark, H.A. Gasteiger, Cathode catalyst utilization for the ORR in a PEMFC, *J. Electrochim. Soc.* 154 (2007) B279–B287.